

Mayday, Mayday, Mayday!




AVIAT-IONS

NASA Space Apps Challenge 2017

Athens, Greece



Athanasopoulos Dimitrios *undergraduate student of Physics*

Chliaras Vangelis *undergraduate student of Physics*

Christopoulou Eleni *undergraduate student of Physics*

Kefala Kyriaki *undergraduate student of Physics*

Konstantinou Anna *undergraduate student of Physics*

Louropoulos Aleksandros *undergraduate student of Physics*

Ntimtsas Aggelos *undergraduate student of Biology*

Palafouta Sofia *undergraduate student of Physics*

Panagiotou Sotiris *undergraduate student of Electrical Engineering*

Papachristou Michalis *graduate student of Astrophysics*

Politopoulos Ioannis *undergraduate student of Physics*

Skretas Iason-Michael *undergraduate student of Physics*

Contents

1. Introduction.....	3
1.1 Cosmic Rays.....	3
1.2 Magnetosphere.....	4
1.3 Particle Injection Probability.....	5
1.4 Solar Energetic Particles.....	7
2. Our Project.....	9
2.1 Atmospheric Model.....	9
2.2 Stopping Power for human body and aircraft fuselage.....	11
2.3 Calculations.....	14
2.4 Web-visualization.....	17
3. Radiation Protection and Aircraft Shielding.....	19
4. Biological Consequences.....	22
5. Future goals.....	23
Appendix.....	24
Bibliography.....	30

1. Introduction

Earth is exposed to galactic and exogalactic radiation. This phenomenon is more intense near the poles due to the geometry of the Earth's magnetic field and atmosphere. Consequently, crew members and passengers of commercial flights are exposed to high rates of radiation.

This project calculates and visualizes this radiation exposure during a certain flight. New models have been developed by our team that take into consideration the interaction of solar particles and cosmic rays with Earth's magnetosphere and atmosphere using data from GOES (Geostationary Operational Environmental Satellite system). The result concerns the dose of radiation at each point of the flight-path and in total. . Finally, this project studies the potential health risks related to this radiation exposure.

1.1 Cosmic Rays

The cosmic rays are a continuous bombardment of extremely energetic charged particles and gamma-photons that approach the earth. Some of them manage to penetrate the Earth's magnetosphere and atmosphere, exposing the crew members and passengers of flights to radiation, which is composed by 80% protons, 15% α -particles whilst the rest 5% is a combination of electrons, heavier ions and photons. They consist of three components: the solar, the galactic and the extragalactic component. While the second and third components are irrelevant to the sun, they appear to have opposite modulation to the solar eleven year cycle (Figure 1). This happens due to the fact that, during the solar maximum, the propagation of the solar wind largely blocks the cosmic rays from entering the heliosphere. The same phenomenon can happen, for smaller timeframes during the low activity period of the sun whenever there is an explosive solar activity such as a flare or a CME.

The only primary cosmic ray particles that can survive transport through the atmosphere and reach cruising altitudes of typical commercial aircrafts are protons with energy on the order of 1GeV or higher. The secondary particles are product of hadronic and electromagnetic showers with energy of 1GeV or higher. The nucleonic component of these secondary particles (protons and neutrons) is the most hazardous for human health, so these are the ones that will be taken into consideration for the calculations in this project. The high LET (Linear Energy Transfer) particles at 10-12km with energy $E < 1\text{GeV}$ are secondary particles, most of them neutrons, created at higher altitudes from nuclear fragmentation reactions. The heavy ions have largely disappeared due to a combination of ionization energy loss and nuclear fragmentation reactions into lower energy lighter particles. The particles with energy much greater than 10GeV, using the power law for cosmic rays $N \sim E^{-2.6}$, have much lower flux, so they do not contribute significantly to the radiation exposure. Therefore, we only take into consideration the cosmic ray protons and the secondary particles, product of hadronic showers (protons and neutrons) in the energy spectrum of $1\text{GeV} < E < 10\text{GeV}$.

For the absorption of cosmic rays the following was used as flux to altitude:

$$F(h) = 10^{\frac{10}{3}} \log(h) - \frac{1}{3} \quad (1.1),$$

where h is the altitude and F is the energy flux.

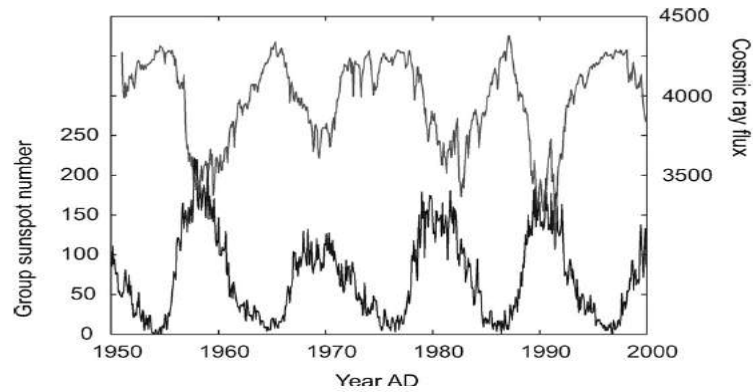


Figure 1. Monthly variation of eleven year cosmic ray cycle (Miyahara H. et al, "Influence of the Schwabe/Hale solar cycles on climate change during the Maunder Minimum", 2009)

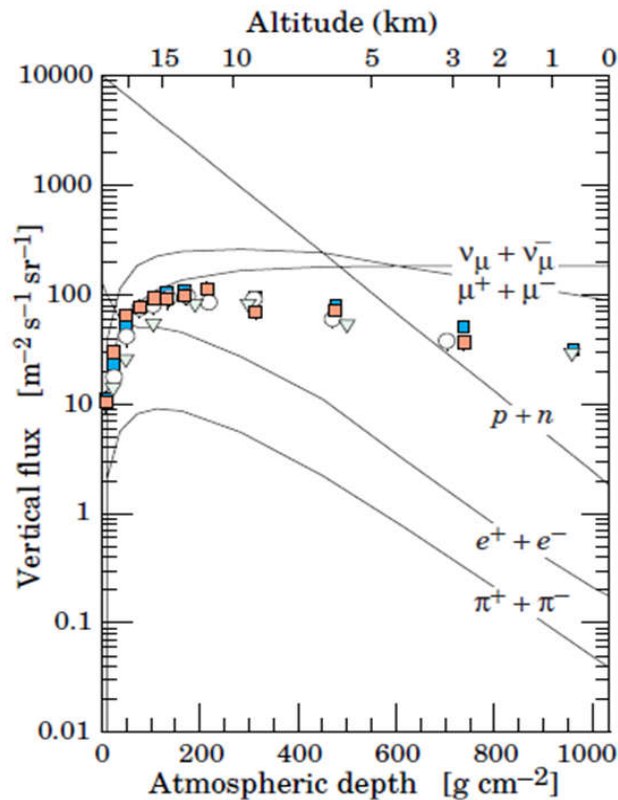


Figure 2. Flux of cosmic ray components as a function of atmospheric depth/altitude. The component that is taken into consideration in this project is the flux of neutrons and protons (Beatty J.J. et al., "Cosmic Rays", 2011)

1.2 Magnetosphere

The Earth's magnetosphere is a region around the planet dominated by the local magnetic field that shields our home planet from solar and cosmic particle radiation, as well as erosion of the atmosphere by the solar wind - the constant flow of charged particles streaming off the sun. The magnetic poles are different from the geographic poles and to be

exact, they are opposite and they have an inclination of 11.5° . Earth's magnetosphere is part of a dynamic, interconnected system that responds to solar, planetary, and interstellar conditions. The Sun facing side - dayside - extends to a distance of about 10 earth radii, whilst the night-side extends up to hundreds of earth radii. There, most of the phenomena of the solar wind start, resulting in particle radiation to the polar cusps, exposing aviation and commercial flights to radiation. This exposure will be discussed in this chapter.

In order to discuss the radiation exposure, all solar phenomena that affect the magnetosphere need to be taken into consideration. The most essential are the CME's, the solar flares and the continuous emission of solar wind towards the earth. These phenomena produce the SEPs (Solar Energetic Particles) that affect our magnetosphere. The intensity of these events goes accordingly to the solar cycle. SEPs -consisting of electrons, rarely protons and in extreme events α -particles - travel through space to our planet along with the solar wind affecting their magnetic properties, energy and dynamic pressure.

Whenever the solar wind meets certain criteria, the particles result in powerful interactions with the magnetosphere such as storms, sub-storms, radiation belts and other. The most essential of these criteria are:

1. Highly energetic solar wind with velocities above 400km/s
2. Southern oriented interplanetary magnetic field
3. The above must last 1-3 hours in case of sub-storms and more than 5-7 hours in case of storms.

During a storm, energy is transported to the magnetotail of earth's magnetosphere, due to magnetic reconnection. After enough energy has been transported, the magnetotail snaps and ejects the plasma trapped in between the magnetic lines towards the earth. A portion of the ejected plasma goes into orbit around the earth, enforcing the ring current, reducing the horizontal component of the magnetic field according to the Dst index. During the recovery phase, the ring current weakens, restoring the magnetic field to its normal values.

The sub-storms are similar dynamic phenomena of smaller scales. The result of these phenomena is the creation of other currents in the magnetosphere and the precipitation of electrons in the atmosphere through the polar cusps. As a result, the spectacular Aurora Borealis and Aurora Australis form. These Auroras are visible due to the ionization of the atmospheric particles such as nitrogen and ozone, that emit "greenish light curtains". A difference between the Aurora Borealis and Aurora Australis is that the former is formed in the southern magnetic pole while the latter is formed in the northern magnetic pole (opposite to the geographic poles). Another difference between the two Auroras is the intensity of their periods due to the inclination of earth's axis to the eclipse plane. During rare events of extremely powerful storms, the Auroras can be visible at lower latitudes.

1.3 Particle Injection Probability

For the purpose of this project, we need to set our focus on the outer radiation belt, in order to calculate and visualize the radiation exposure of commercial flights, which operates in altitudes of 5-12 km. This radiation belt is mostly toroidal and lies in 3-5 Earth radii consisting mostly of electrons with energy of 0.1-10MeV. The magnetic shells that create

this belt are connected to high magnetic latitudes on the Earth's surface. Some sample values for quiet Sun are:

- $L=3$ corresponding to latitude $\lambda=67.5^\circ$
- $L=4$ corresponding to latitude $\lambda=72^\circ$
- $L=5$ corresponding to latitude $\lambda=78^\circ$

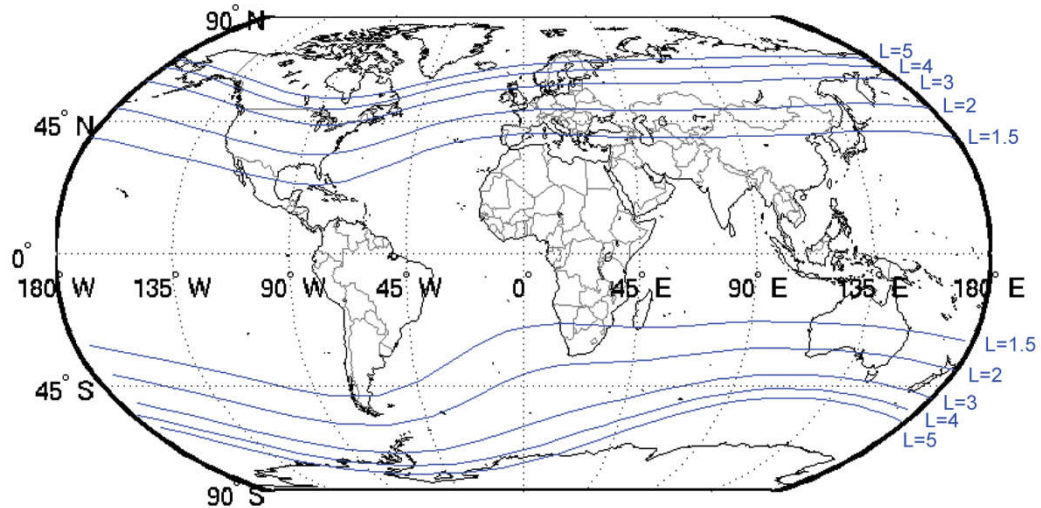


Figure 3. Earth magnetic latitudes and longitudes (© Daniel I Golden)

The electrons of the outer belt move around the magnetic lines through the Larmor effect (gyromotion) preserving the first adiabatic invariant. Simultaneously, they move parallel to magnetic lines, bouncing between two mirror points where the pitch angle becomes 90° . The equation for the pitch angle is given below:

$$\alpha = \arctan \frac{v'}{v} \quad (1.2),$$

where v' corresponds to perpendicular component and v corresponds to the parallel (to the magnetic line) component of the velocity.

Moving towards higher latitudes, the pitch angle increases and the particle bounces when α reaches 90° . However, in some cases the pitch angle does not reach the value of 90° . Such cases are:

1. Pitch scattering: the shift of the pitch angle due to interactions with low frequency electromagnetic waves $\sim 1\text{Hz}$
2. Loss cone: when the pitch angle in the equatorial plane is less than critical value which can be calculated by the following equation:

$$\sin^2 \alpha_0 = (4L^6 - 3L^5)^{-\frac{1}{2}} \quad (1.3),$$

As a result, the second adiabatic invariant is not preserved and the particle doesn't bounce, so it falls in the atmosphere through the polar cusps following the magnetic line. The electrons that actually fall into the atmosphere, are the ones that have a pitch angle lower than the equatorial pitch angle. Assuming that the pitch angle is homogenous among

the energy spectrum of electrons, then the percentage that fall into the atmosphere is given by the equation $\alpha < \alpha_0$. The probabilities according to the L are:

- L=3 → Probability=9.3428%
- L=4 → Probability=5.9354%
- L=5 → Probability=4.1963%

These probabilities are one of the factors we used for the calculation of the flux of the electrons falling into the atmosphere.

The GOES satellite is located in geostationary orbit so for the measurements and calculations the probability for L=5 will be used.

1.4 Solar Energetic Particles

Solar energetic particles (SEP) are high-energy particles coming from the Sun and were first observed in the early 1940s. They consist of protons, electrons and ions with energy ranging from a few tens of KeV to GeV. SEPs can originate either from a solar-flare site or by shock waves associated with coronal mass ejections (CMEs). However, only about 1% of CMEs produce strong SEP events (*Christian E.R., "Coronal Mass Ejections", NASA/Goddard Space Flight Center, 2012*).

SEPs can be accelerated to energies of several tens of MeV within 5-10 solar radii (5% of the Sun–Earth distance) and can reach Earth in a few hours. Two main mechanisms of acceleration are possible: diffusive shock acceleration or shock-drift mechanism. This makes prediction and warning of SEP events quite challenging.

In case of SEP events, highly energetic protons may penetrate into the same magnetic shells and follow the same process resulting in falling into the atmosphere. A solar particle event is a period of heightened SEP flux, usually arriving at Earth tens of minutes after the associated solar event and lasting 1 to several days. During a solar particle event, protons with energies up to 10MeV penetrate below ~100 km altitude producing ionization in the Polar Regions. The more energetic ions penetrate deep into the Earth's middle atmosphere to ~12–80 km causing changes in atmospheric constituents and dynamics [Jackman et al., 2005; Clilverd et al., 2005].

Cutoff latitude

The lowest latitude to which an energetic solar ion can penetrate is known as its cutoff latitude, and is a function of the ion's momentum per unit charge, which is referred to as its rigidity. One may consider a cutoff rigidity corresponding to a given location within the geomagnetic field. The cutoff rigidity is the minimum rigidity particle with access to that location. Surfaces of constant cutoff rigidity in the magnetosphere approximately follow surfaces of constant L shell. During quiet geomagnetic periods, the cutoff latitudes for most SEPs fall over a small range of latitudes near ~60° International Geomagnetic Reference Field (IGRF) invariant latitude, which corresponds to $L \sim 4$. During a geomagnetic storm the Earth's field is distorted modifying SEP access to the inner magnetosphere. At the main phase of the storm, the cutoff latitude can be suppressed up to ~15° equatorward, exposing normally shielded midlatitudes to radiation and increasing the polar cap area to which SEPs have access by a factor of 2–3 [Labrador et al., 2003].

Cutoff latitude correlation to Dst and Kp indices

As shown in (Lesk et al., 2001), the effect of cutoff latitude in geomagnetic activity can be seen through the Kp and Dst indices, both of which are readily available or forecast in near real time. Significant variations in the cutoff location often by $\sim 5^\circ$ - 10° in less than a day, are clearly seen. In general, the shapes of the time variations in the cutoff are remarkably well correlated with corresponding changes in Dst, even down to small amplitudes ($<1^\circ$) and short (several hour) timescale. In cases of geomagnetic storms though, the Kp index responds before Dst therefore it may be that the sudden cutoff suppressions are better correlated with Kp. A change in Dst by 200nT during a major geomagnetic storm moves the cutoff latitude by $\sim 8^\circ$ - 10° for these ~ 8 -15 MeV/nucleon He nuclei (which have a rigidity of ~ 250 -340 MV, equivalent to ~ 30 -60 MeV protons).

2. Our Project

Existing atmospheric models and models for radiation absorption were not accessible or didn't match the needs of our project. As such, we decided to develop a new atmospheric model, a model for the flux of particles arriving to the atmosphere and a model for the absorption of radiation in it. The created models are described in the next paragraphs.

2.1 Atmospheric model

In the developed atmospheric model, the following are assumed:

- Protons with energy less than 1GeV are ignored, as stated in paragraph 1.1
- The atmospheric limit is at an altitude of 100km, which is a part of the ionosphere where the absorption of particle radiation is considerable.
- The chemical composition is the same along the atmosphere but the density is different
- The flux that arrives at the atmospheric limit is the same as the flux measured with the GOES Satellite.

According to the "U.S. Standard Atmosphere 1976", the density decreases exponentially with altitude, as it is presented below.

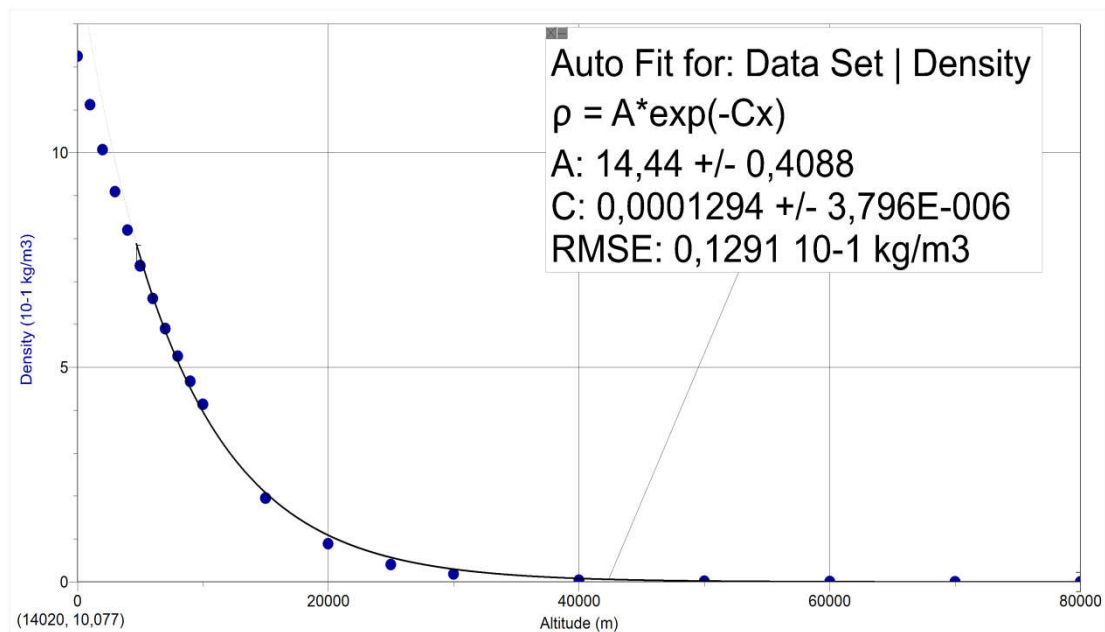


Figure 4. Density-altitude function.

$$\rho = 14.44 \cdot \exp(-0.0001294 \cdot h) \quad (2.1)$$

The atmosphere is considered as an ellipsoid where the semi-major axis is the altitude at the equator and the semi-minor axis is the altitude at the poles. For this consideration, the atmospheric limit altitude is linearly proportional to the tropopause limit at the equator and the poles. The atmospheric limit is at 100km for the equator and at 35km for the poles.

The calculations indicate that stopping power is constant in regard to altitude, using data from http://www.engineeringtoolbox.com/standard-atmosphere-d_604.html (accessed Sunday 30/04/2017). The results are shown below:

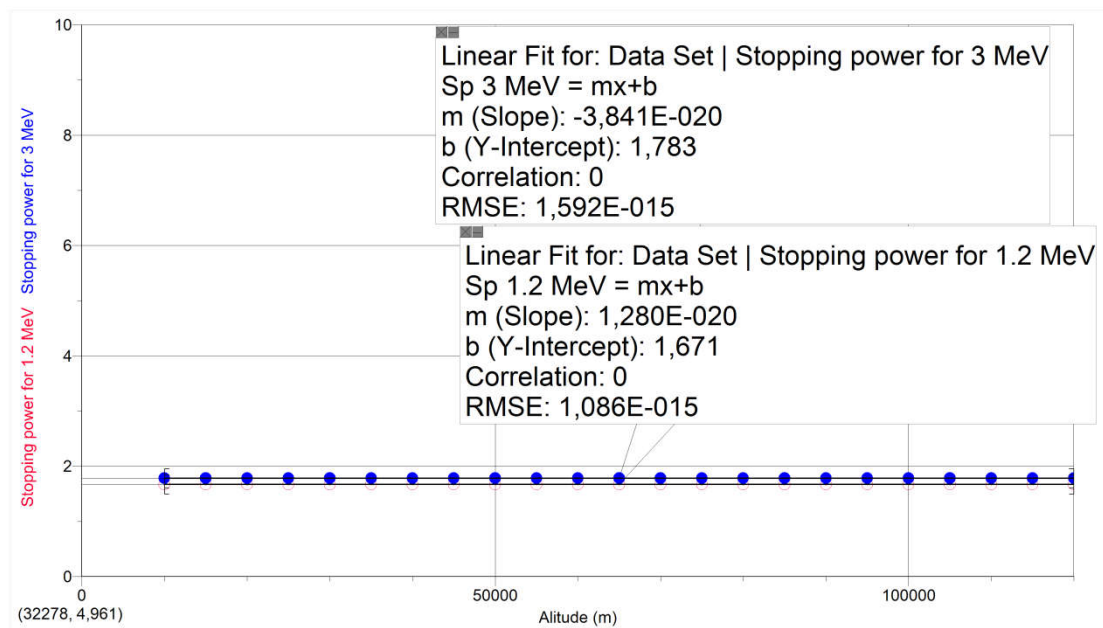


Figure 5. Stopping power in function of altitude is considered constant

The definition of stopping power is $S = -\frac{dE}{dx}$ (2.2). The stopping power of electrons is shown in the following table.

Chart 1. Stopping Power of electrons calculated for different energies

Energy (MeV)	1,5	3	4
Stopping Power $\left(\frac{MeV \cdot cm^2}{gr}\right)$	1,671	1,783	1,85

Using the stopping power, the energy flux of each particle at the limit of the atmosphere and the atmospheric model, the energy at any altitude can be calculated using the following equation:

$$S = -\frac{dE}{dx} \rightarrow dE = -S \cdot dx \rightarrow E = E_0 - \int S \cdot dx \rightarrow F = F_0 - \int \frac{S \cdot \rho(h) \cdot dx}{\delta\alpha \cdot \delta t \cdot \delta\Omega} \quad (2.3),$$

where F is the energy flux at any altitude, F_0 is the energy flux at the atmospheric limit, S is the Stopping Power in MeV/cm, X is the distance to the atmospheric limit, S' is the Stopping Power in MeV cm²/gr, ρ is the atmospheric density, h is the altitude and $\delta\alpha = 1\text{cm}^2$.

For latest Auroral predictions we used data from NOAA, Space Weather Prediction Center at <http://services.swpc.noaa.gov/text/aurora-nowcast-map.txt> through the website <http://www.swpc.noaa.gov/products/aurora-30-minute-forecast>.

As for the meteorological phenomena, they take place beneath the flight altitude and, as such, are not included in the model. However, increases and reductions of the air density do happen in those heights due to air currents and such currents will be added in the future.

2.2 Stopping power for human body and aircraft fuselage

The stopping power for the human body was calculated using the same method. The chemical components used in the application are:

Chart 2.Components of human body and percentage in human body

Chemical Component	Oxygen	Carbon	Hydrogen	Nitrogen	Calcium	Polonium
Percentage (%)	0.65	0.185	0.095	0.032	0.015	0.01

For each energy spectrum, the stopping power is shown in the following diagrams. Values were calculated analytically with ESTAR (See Appendix) and we used them in order to fit an equation for each case.

- Electrons

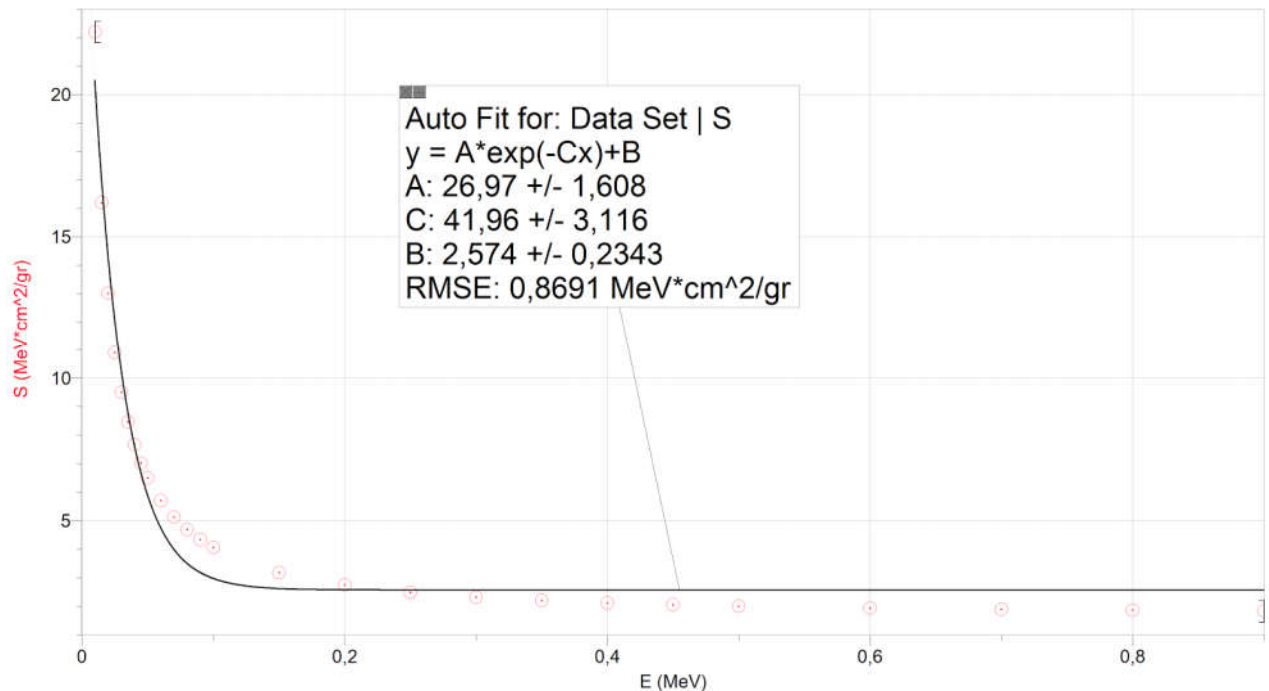


Figure 6.Stopping power of electrons with E<1MeV

$$S(E<1\text{MeV}) = 26.97 \cdot \exp(-41.96 \cdot E) + 2.574 \quad (2.4)$$

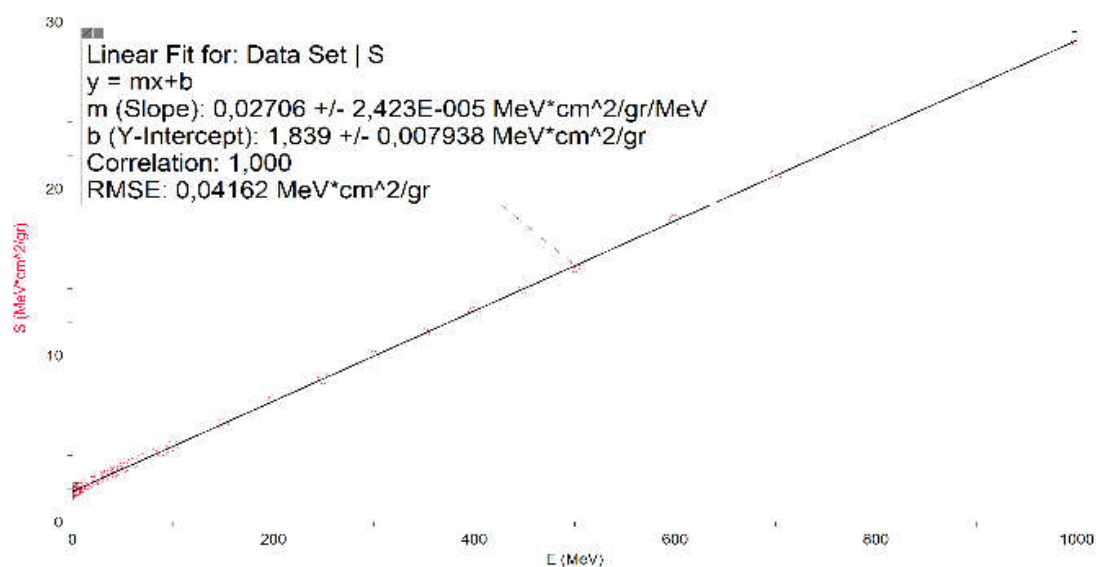


Figure 7. Stopping power of electrons with $E \geq 1 \text{ MeV}$

$$S(E \geq 1 \text{ MeV}) = 0.02706 \cdot E + 1.839 \quad (2.5)$$

- Protons

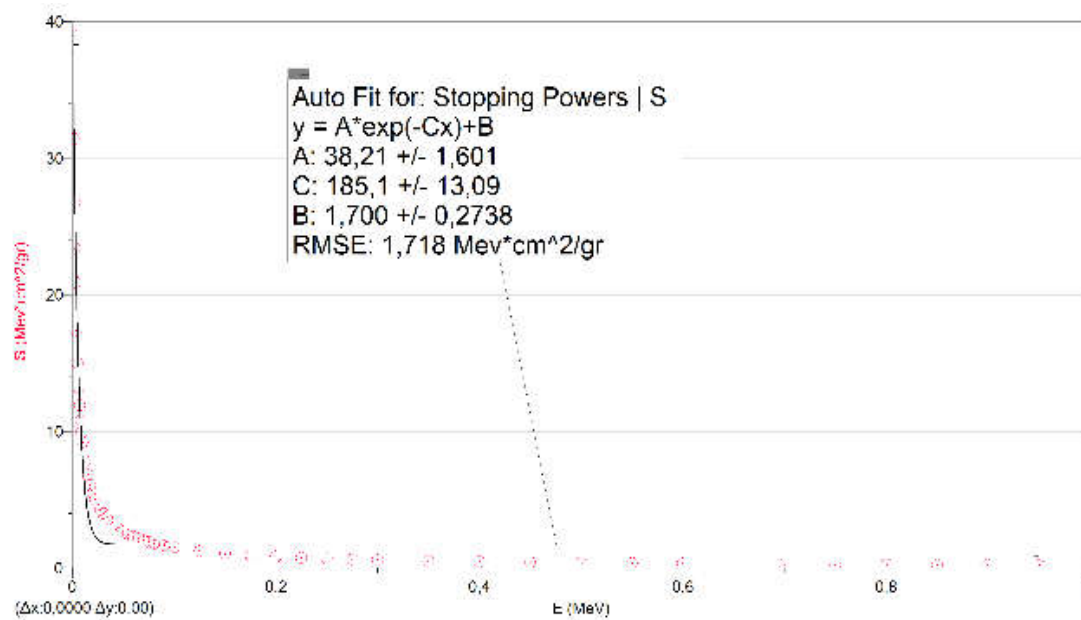


Figure 8. Stopping power of protons with $E < 1 \text{ MeV}$

$$S(E < 1 \text{ MeV}) = 38.21 \cdot \exp(-185.1 \cdot E) + 1.7 \quad (2.6)$$

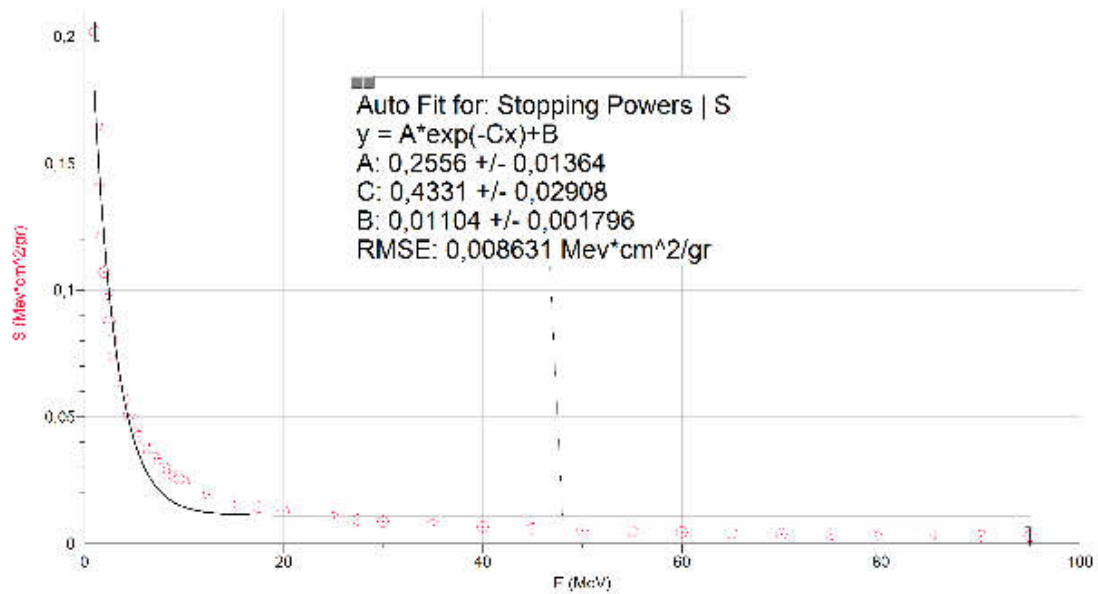


Figure 9. Stopping power of protons with $1 \leq E < 100 \text{ MeV}$

$$S(1 \text{ MeV} \leq E < 100 \text{ MeV}) = 0.2556 \cdot \exp(-0.4331 \cdot E) + 0.01104 \quad (2.7)$$

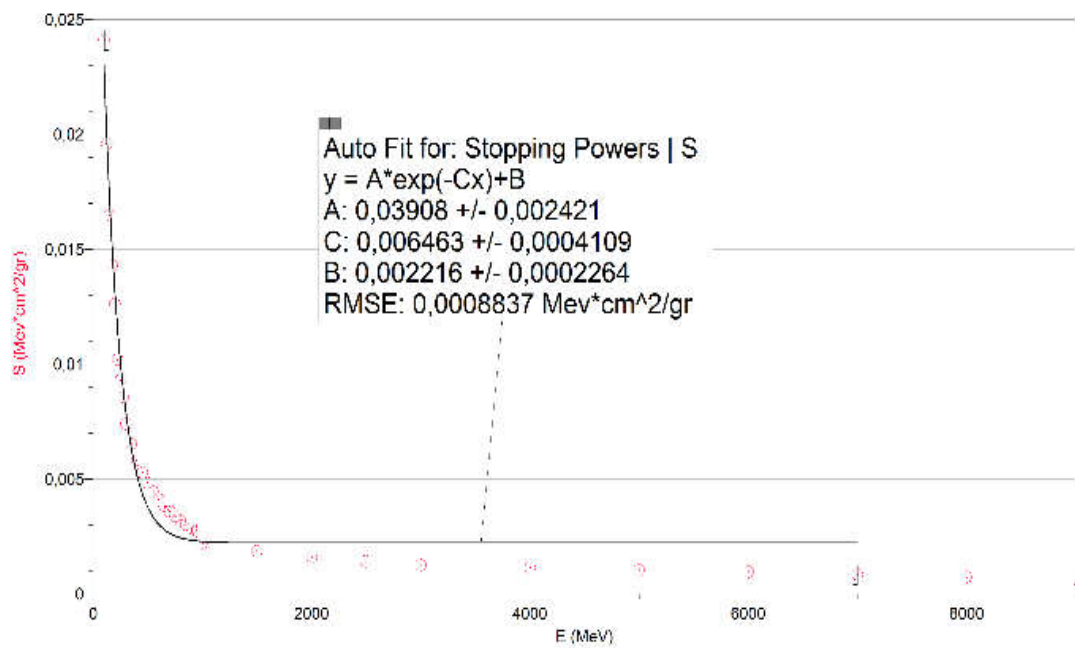


Figure 10. Stopping power of protons with $E \geq 100 \text{ MeV}$

$$S(E \geq 100 \text{ MeV}) = 0.03908 \cdot \exp(-0.006463 \cdot E) + 0.002216 \quad (2.8)$$

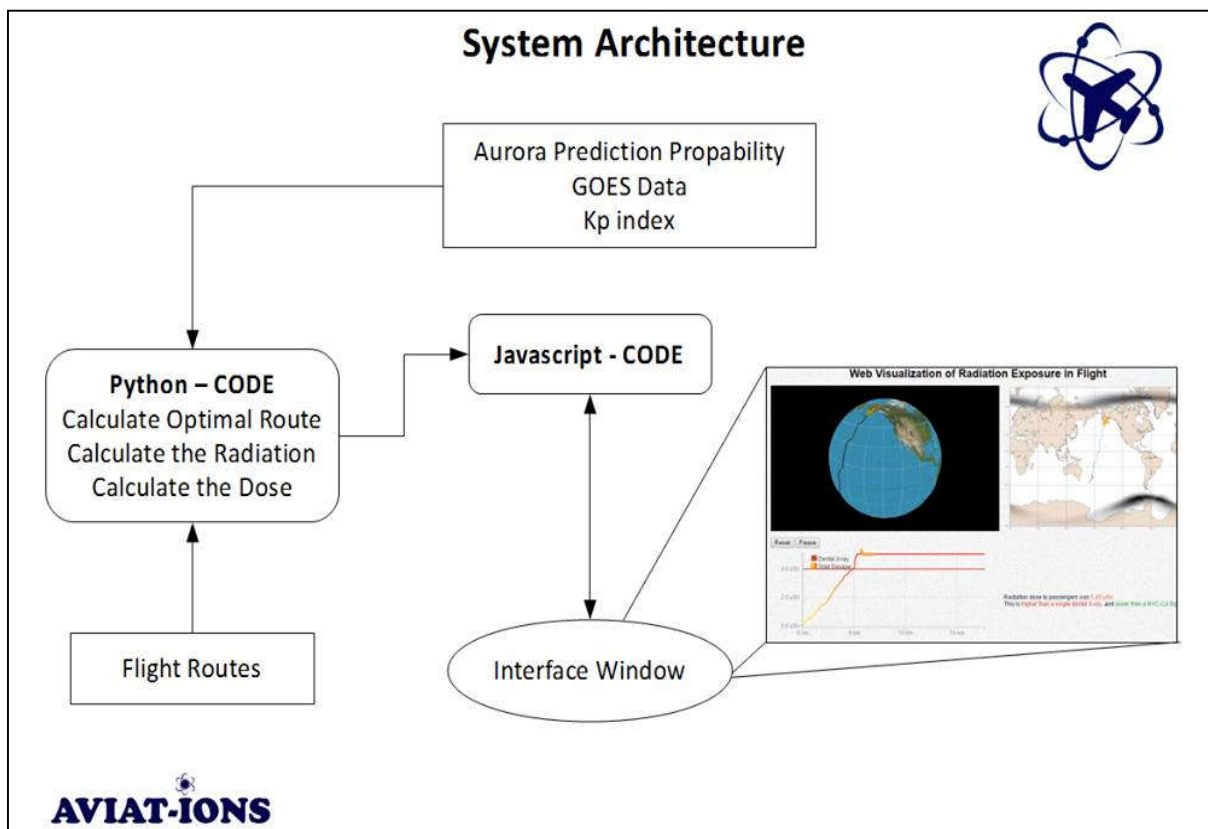
Stopping power for aircraft fuselage

The material of aircraft's fuselage with the highest stopping power value is aluminum. Our hypothesis is that the total aluminum thickness of fuselage's shell is 5cm. Using the "estar" online application, the stopping power value is the following:

- For cosmic ray protons that fall on the fuselage with energy of $\sim 100\text{MeV}$, the stopping power is $S=50.139\text{MeV}\cdot\text{cm}^2\cdot\text{gr}^{-1}$.
- For outer radiation belt electrons with energy of $\sim 1\text{MeV}$, the stopping power is $S=2.322\text{MeV}\cdot\text{cm}^2\cdot\text{gr}^{-1}$.

2.3 Calculations

The sequence of steps is described briefly in the flowchart.



The full calculation code is given in the link:

<https://github.com/ax3l91/space-apps-2017-mayday-athens/blob/master/Kp.ipynb> .

It takes into consideration all the factors explained in the project. As input, it takes the Kp index, flight routes, live GOES Satellite flux data, Aurora prediction data (just for display). The Kp index, GOES Satellite flux and aurora prediction **live data**, are pulled from their sources **once every hour**. So, for a given flight path, the program can generate results every hour.

GOES satellite electron flux data: <http://services.swpc.noaa.gov/text/goes-particle-flux-primary.txt>
 kp index: <http://legacy-www.swpc.noaa.gov/wingkp/index.html>

It simulates the flight route and the radiation effects that are encountered and outputs the total radiation dose for an average human, the time series of exposure during the flight and a physical simulation in 3D world model.

The code that executes the calculations uses the GOES satellite electron flux data to calculate the energy flux at the atmospheric limit. To calculate this we need the electron flux F_k^G multiplied by the probability of an electron falling into the atmosphere due to its pitch angle P and by the energy channel k E_k .

$$F_k = F_k^G \cdot P \cdot E_k \quad (2.9)$$

In order to calculate the energy flux that reaches a human inside an aircraft at a commercial flight altitude, we used our own developed model for atmospheric and airplane fuselage absorption. To calculate the stopping power of the airplane fuselage, the same online application as for atmospheric stopping power was used, considering that the energy flux is absorbed mostly by its 6-10cm thick aluminium shell. The formula used for the calculations is the following

$$F_k(h, \phi) = F_k \cdot \Lambda \cdot (S_k \int_h^{H(\phi)} \rho(z) dz - S_a \cdot \rho_a \cdot d_a) \quad (2.10),$$

where $F_k(h, \phi)$ is the energy flux at any altitude h and every latitude ϕ , Λ is a unit conversion factor, S_k is the atmospheric stopping power for k -channel energy spectrum (see paragraph 2.2), $\rho(z)$ is the atmospheric density, S_a , ρ_a and d_a are the stopping power, density and fuselage thickness respectively. Now, we are able to calculate the dose $D(h, \phi)$ for a crewmember or passenger of a commercial airplane with a biological stopping power S_b . (K is a unit conversion factor)

$$D(h, \phi) = 2\pi K \left(\sum_{k=1}^3 F_k(h, \phi) \cdot S_b \cdot (F_k^G \cdot P) - 1 \right) \quad (2.11)$$

Using the K_p index, we can calculate a maximum ϕ_{max} under which we accept that all radiation is absorbed and therefore the dose is zero for any altitude, $D(h, \phi < \phi_{max}) = 0$.

For the calculation of cosmic ray flux, as described in 1.1 we used the equation

$$F(h) = 10^{\frac{10}{3}} \cdot \log(h) - 13 \quad (2.12),$$

where $h = h(\phi)$ and, as expected, its value is many orders of magnitude lower than the outer radiation belt energy flux. An algorithm to optimize the flight path, in order to minimize the total radiation dose proportionally to flight distance, is under construction. To do this we are going to try to minimize a cost function of the form:

$$f(X) \sim (\text{Distance}(X) \cdot \text{Dose}(X))^2 \quad (2.13),$$

where X is a vector of the flight path.

We are going to try 3 methods to do this. First by using a bigger flight path (assuming that the initial path is a great circle between two points in the globe) and calculating its cost function.

The second method is by using a gradient descend algorithm for our cost function with constraints about initial and last point of the route. We have already started testing this method with no sufficient results yet.

The last method we are going to try is minimizing our cost function by using the flight path as a “chromosome” in a genetic algorithm. The stochastic behavior of such an algorithm may give us better results than gradient descent methods because the bigger distances from the starting minimum distance path creates a “barrier” in our cost function.

Results for one flight

For the flight plan <https://flightplandatabase.com/plan/347165> (accessed at 30/4/2017), the above calculations were executed and the results are shown in the following diagrams.

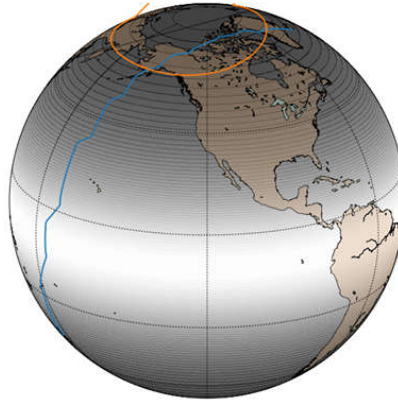


Figure 11. Depiction of flight path (blue line), the lowest limit in which solar radiation is taken into account (orange circle), radiation dose globally (grey)

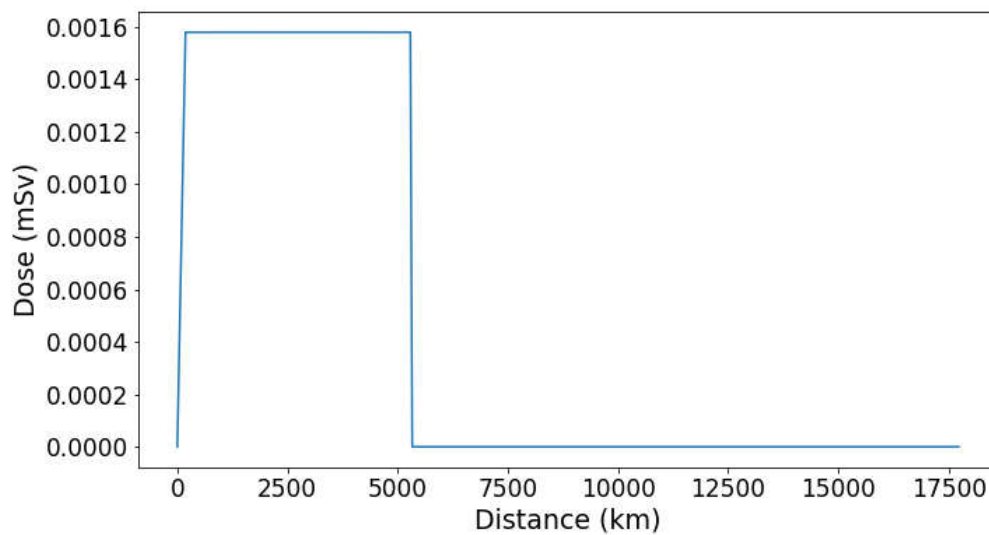


Figure 12. Dose at each point of the flight path

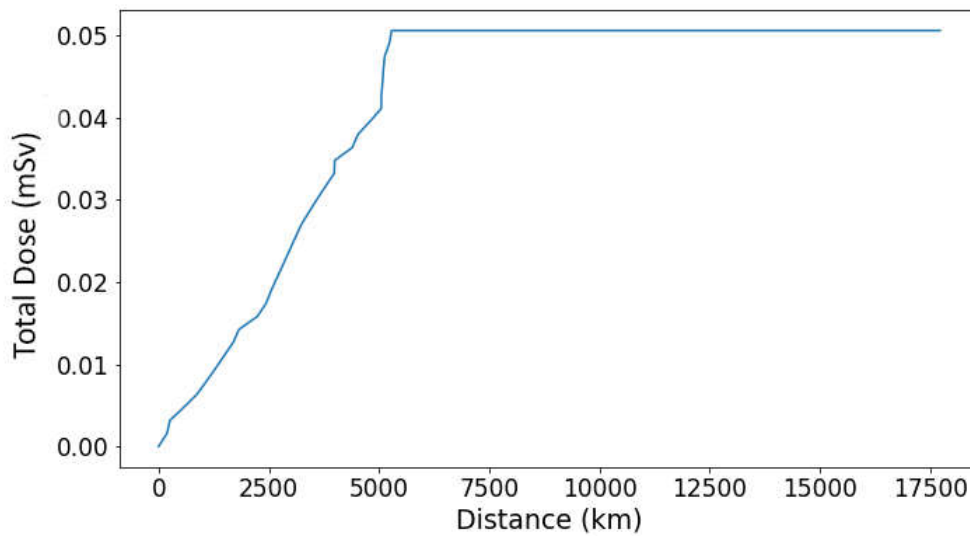


Figure 13. Total dose in a near polar flight

For this flight plan, the total dose value is less than radiation dosimetry limit and there are no biological consequences as shown in chapter 3.

2.4 Web-visualization

The full visualization code is given in the link:

<https://github.com/ax3l91/space-apps-2017-mayday-athens/blob/master/Kp.ipynb>

Besides the visualization given at Kp.ipynb, the browser provides a front end that pulls the simulation data and visualizes them in user friendly form.

The web-visualization is split in four parts:

1. 3D visualization of the globe with the simulated flight path pseudo-colored, according to the radiation intensity at each point.
2. 2D visualization of the world map marking the flight path and showing the expected aurora probability at each point.
3. Live chart of the cumulative radiation dose of the flight path to the distance traveled. The user can hover over the line of the chart to get exact values of time and total radiation dose value for a point in time.
4. Total radiation dosage and generated comments on the health aspects of the simulated flight in an understandable way for the public, with examples out of the everyday life.

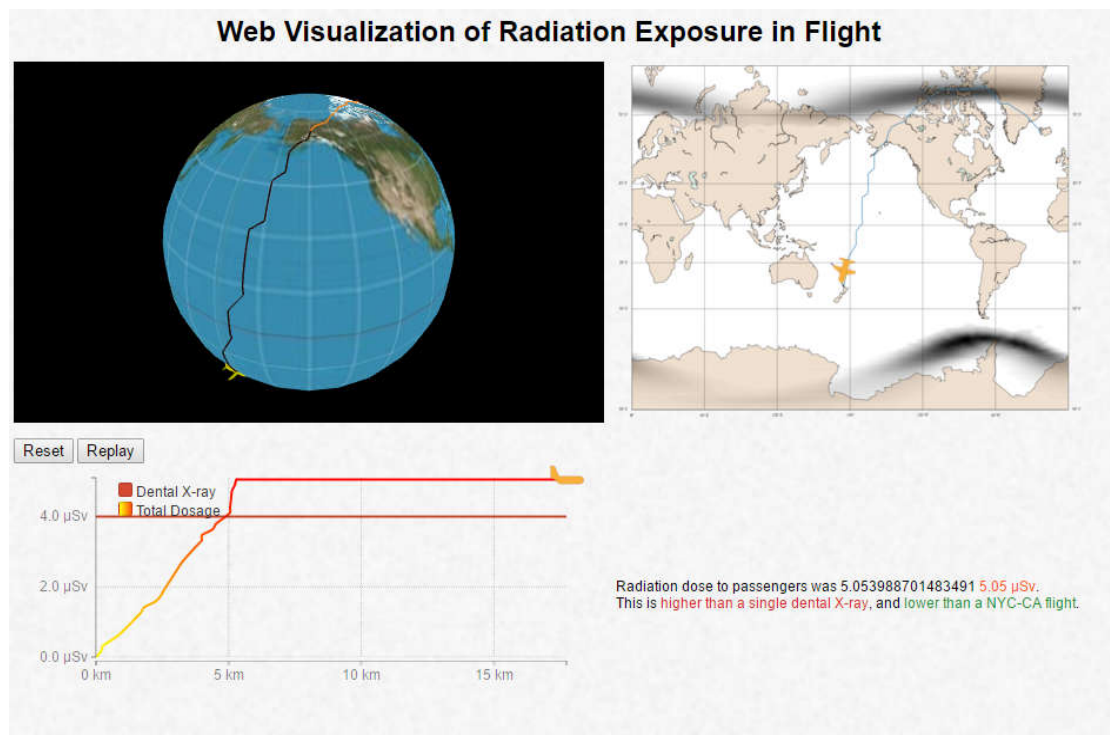


Figure 14.Result of our code. Up: Path of flight in 3D and 2D Down: Total Dose

3. Biological consequences

One of the most important applications of the above results is the biological impact of the radiation exposure on the human body. Therefore, it is highly important to calculate the dose of radiation a human body can stand and the dose of radiation it actually receives during a flight, in order to predict possible biological damages and impacts and get the necessary protection.

Firstly, almost 99% of the mass of the human body is made up of six elements: oxygen (O₂), carbon(C), hydrogen(H), nitrogen(N), calcium(Ca), and phosphorus(P). Only about 0.85% is composed of another five elements: potassium, sulfur, sodium, chlorine, and magnesium. All eleven are necessary for life.

The radiolysis of water due to ionizing radiation, results in the production of electrons, H atoms, OH radicals, HO⁺ ions and molecules (dihydrogen H₂ and hydrogen peroxide H₂O₂). Radiolysis is an indirect way of energy transfer into biomolecules. The products of radiolysis, free radicals such as H₂O₂ on high concentrations are toxic for the cells because they have the ability to oxidize organic compounds. Research connects the existence of free radicals with premature aging, cancer, respiratory problems, even failure at ATP production from mitochondria. If a big number of cells drive into apoptosis or necrosis then we have organ failure and finally death (Sophie Le Caër, *“Water Radiolysis: Influence of Oxide Surfaces on H₂ Production under Ionizing Radiation”*, Giorgio M et al., *“Hydrogen peroxide: a metabolic by-product or a common mediator of ageing signals?”*, 2007, López-Lázaro M, *“Dual role of hydrogen peroxide in cancer: possible relevance to cancer chemoprevention and therapy”*, 2007, Rapoport R. et al. *“A fluorimetric assay for hydrogen peroxide, suitable for NAD(P)H-dependent superoxide generating redox systems.”*).

The direct way of energy transfer can cause physical and chemical changes in proteins, lipids and DNA. The cell is “armored” with specialized repair mechanisms and they can repair that change. However, sometimes they aren’t available to repair the damages and finally the cell continues to live with the damages (the beginning of cancer issues) or dies (apoptosis).

The severity of the molecular damage caused is directly related to the degree of ionization produced by the radiation in the biological tissue, i.e. by the rate at which radiation radiates its energy. A relative magnitude that quantifies the energy deposit rate is Linear Energy Transfer (LET) defined as the energy transfer rate in a particular area of matter.

$$LET = \frac{dE(absor)}{dx} \text{ (KeV/}\mu\text{m)} \quad (3.1)$$

→The increase of LET value implies more biological damage.

(Symeopoulos B. (2016), *“Radiobiology for undergraduate students”*)

Using the stopping power for human body and flux at the flight altitude, it is now possible to calculate the effective dose using the radiation dosimetry equation

$$D = K \int_{\Omega} \int_0^{\infty} S_j(E) \Phi_j(x, \Omega, E) d\Omega dE \quad (3.2),$$

where D is the energy deposited in a target medium by the radiation field of particle j, which is the dose. In the above equation, S_j(E) is the target stopping power for particle j (MeV/g/cm²) and K is a unit conversion factor (1,602x10⁻¹⁰).

Dose equivalent in tissue T from particle j (H_j, T(x)) is defined in terms of the tissue LET dependent quality factor Q, such that

$$H_{j,T}(x) = \int_L Q(L)D_j(x,L)dL \quad (3.3),$$

where L is LET, which can be approximated by the stopping power in units of KeV/um; $D_j(x,L)$ is the spectral dose distribution from particle j in terms of LET, and $Q(L)$ is the tissue LET-dependent quality factor.

The relationship between the probability of biological damage and dose equivalent is found to be also depended of the organ or tissue irradiated. A further dosimetric quantity, called the effective dose, is defined to include the relative contributions of each organ (w_T) or tissue to the total biological detriment caused by radiation exposure. The effective dose $E(x)$ is the sum of weighted dose equivalents in all the organs and tissues in the human body, such that

$$E(x) = \sum_T \sum_j w_T H_{j,T}(x) \quad (3.4)$$

In addition, during a flight there are some exposure variables that must be considered such as the time of exposure during an air flight, the age and the health background of each pilot and a possible pregnancy.

The side effects of exposure in radiation variate accordingly the exposure variables. Crewmembers are exposed to low-level cosmic ionizing radiation. Annual effective doses for flight crew have been estimated to be in the order of 2-5mSv and can attain 75mSv at career end. The last 15–20 years, epidemiological studies usually focus on radiation-associated cancer. These studies concluded that the overall cancer risk was not elevated in most studies and subpopulations analyzed, while malignant melanoma, other skin cancers and breast cancer in female aircrew have shown elevated incidence, with less risk elevations in terms of mortality. In some studies brain cancer risk appears elevated. Cardiovascular mortality risks were generally very low.

In a near-polar or polar flight the possibility for crewmembers to have serious cancer problems is very low. A pilot during the flight can receive electrons with energy 0.1-1 MeV and rarely (according to the above) protons and neutrons with 1 GeV energy. The skin (with subcutaneous tissue) thickness for an average human is 9.96mm.

The density-thickness value for the outer layer of dead skin of the human body is 7 milligrams per square centimeter (mg/cm^2) or $0.007 \text{ g}/\text{cm}^2$.

(J. M. Thomas, R. S. Bogard (1994) "Technical Basis for Beta Skin Dose Calculations at the Y-12 Plant")

Electrons

There exists an approximate empirical relationship between range and energy for low energy electrons

$$r = \frac{0.142 \text{ g}/\text{cm}^2}{\rho} E^{1.29} \quad (3.5),$$

where r is in cm, E is in MeV, and ρ is the density of the stopping material in g/cm^3

- *Electrons with 0.1MeV energy have a range of 1.04cm in skin tissue*
- *Electrons with 1 MeV energy have a range of 20.3 cm in skin tissue*

As such, beta particles can penetrate the dead layer of skin and cause serious problems, especially the electrons with 0.1MeV energy because they stop in skin layer. At this point it is crucial to mention that the results of our calculations may differ in reality due to biological factors.

Consequently, the particles will stop inside the layer of the skin and maybe this is the reason for skin and breast cancer issues.

4. Radiation Protection and Aircraft Shielding

The amount of dose of radiation received while flying depends on the duration of the flight, the altitude, the latitude and of course the solar activity. Lowest dose rates at a given altitude are found near the equator and at short time flights, and increases at long time flights and approaching the poles (higher altitude leads to higher dose rate). Passengers and crew members, in order to reduce exposure to cosmic radiation, should avoid long flights, flights at high latitudes or near-pole flights. Full elimination of exposure to solar particle events is difficult, because we usually cannot have quick and valid predictions, but the received dose can be optimized through appropriate aircraft shielding.

Investigations have been made in order to find appropriate materials for the aircraft. The first material contains a large amount of hydrogen and thereby guarantees an efficient slow down and energy loss of very fast neutrons by means of elastic collisions, a process called thermalization. Its efficiency relies on the fact that neutrons have nearly the same mass as hydrogen nuclei (protons) and as a result in each collision a maximum of their kinetic energy is transferred to the hydrogen nuclei. The second constituent of the shielding solution is characterized by a high ability to absorb slow, thermal neutrons such as boron or compounds.

When it comes to the first shielding component required to attenuate highly energetic neutrons, one natural way would be to use liquid with cryoplane technology. LH₂ is a material that provides a long-term technological option as alternative fuel. It must be cooled down to the liquid state and thus necessitates very good insulation of the tanks or pipes. For this reason, new aircraft configurations are required.

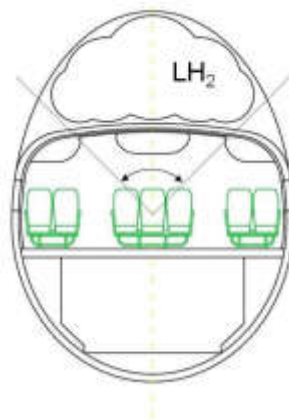


Figure15. Model of cryoplane technology with LH₂ for aircraft shielding (Schrempp L., Sizmann A., Luftfahrt B. (2012), "SHIELDING COSMIC RADIATION IN AIR TRAFFIC").

Candidate materials for neutron protection include thin graphite epoxy skins bonded to an aluminium honeycomb core, composite materials with a polymeric phase, featuring neutron-absorbing particle inclusions, traditionally of micrometer size. However, it has been shown that better shielding requires nanometer range. Such nano-composites could be applied as millimeter-thin films, foams or pastes to the ceiling of an aircraft's cabin interior.

5. Future goals

- Take into consideration improved models of GCR and SEPs.
- Include a more detailed model of magnetosphere dynamics.
- Improve the code to take into consideration magnetic anomalies of the earth's magnetic field like the South Atlantic Anomaly.
- Improve the created atmospheric model to take into consideration atmospheric weather phenomena and conditions at flight altitudes as well as air currents above them.
- Create a mini device to put into aircrafts for in situ measurements in order to avoid a sudden substorm/storm.
- Use existing models of hadronic and electromagnetic shower to further improve the total energy flux at flight altitude.
- Considerate 11 year cycle in order to include the change in rate of cosmic rays and SEPs.
- Create Monte Carlo simulations for pitch angle.
- Make a detailed airplane shielding model, for different types of airplanes depending on airplane's fuselage, to protect crew members and passengers from the radiation exposure.
- Make a full web application allowing the user to choose a flight of his own, existing or not (Dynamic flight selection).
- Improve code to optimize any flight path to minimize the radiation dose proportionally to flight distance.

Appendix

A1. Stopping power for protons and electrons calculated from ESTAR- an online free software.

Protons	MS20 Tissue Substitute					
	Stopping Power			CSDA Range (g/cm ²)	Radiation Yield	Density Effect Parameter
	Kinetic Energy (MeV)	Electronic	Nuclear	Total		
	1,00E-03	1,74E+02	3,90E+01	2,13E+02	5,71E-06	0,4699
	1,50E-03	2,14E+02	3,14E+01	2,45E+02	7,87E-06	0,5104
	2,00E-03	2,47E+02	2,67E+01	2,73E+02	9,80E-06	0,5424
	2,50E-03	2,76E+02	2,34E+01	2,99E+02	1,16E-05	0,5685
	3,00E-03	3,02E+02	2,09E+01	3,23E+02	1,32E-05	0,5902
	4,00E-03	3,45E+02	1,74E+01	3,62E+02	1,61E-05	0,6251
	5,00E-03	3,83E+02	1,50E+01	3,98E+02	1,87E-05	0,6523
	6,00E-03	4,18E+02	1,32E+01	4,31E+02	2,11E-05	0,6742
	7,00E-03	4,49E+02	1,19E+01	4,61E+02	2,34E-05	0,6923
	8,00E-03	4,78E+02	1,08E+01	4,89E+02	2,55E-05	0,7077
	9,00E-03	5,04E+02	9,93E+00	5,14E+02	2,75E-05	0,7211
	1,00E-02	5,29E+02	9,21E+00	5,38E+02	2,94E-05	0,7327
	1,25E-02	5,78E+02	7,81E+00	5,86E+02	3,38E-05	0,7567
	1,50E-02	6,20E+02	6,82E+00	6,27E+02	3,79E-05	0,7755
	1,75E-02	6,56E+02	6,06E+00	6,62E+02	4,18E-05	0,7908
	2,00E-02	6,88E+02	5,47E+00	6,94E+02	4,55E-05	0,8035
	2,25E-02	7,17E+02	5,00E+00	7,22E+02	4,90E-05	0,8143
	2,50E-02	7,42E+02	4,60E+00	7,47E+02	5,24E-05	0,8237
	2,75E-02	7,64E+02	4,27E+00	7,69E+02	5,57E-05	0,832
	3,00E-02	7,84E+02	3,99E+00	7,88E+02	5,89E-05	0,8393
	3,50E-02	8,19E+02	3,53E+00	8,23E+02	6,51E-05	0,8517
	4,00E-02	8,49E+02	3,17E+00	8,52E+02	7,11E-05	0,862
	4,50E-02	8,73E+02	2,88E+00	8,76E+02	7,69E-05	0,8707
	5,00E-02	8,92E+02	2,65E+00	8,95E+02	8,25E-05	0,8781
	5,50E-02	9,06E+02	2,45E+00	9,09E+02	8,81E-05	0,8846
	6,00E-02	9,17E+02	2,28E+00	9,19E+02	9,36E-05	0,8904
	6,50E-02	9,24E+02	2,14E+00	9,26E+02	9,90E-05	0,8956
	7,00E-02	9,28E+02	2,01E+00	9,30E+02	1,04E-04	0,9003
	7,50E-02	9,29E+02	1,90E+00	9,31E+02	1,10E-04	0,9045
	8,00E-02	9,29E+02	1,80E+00	9,31E+02	1,15E-04	0,9084
	8,50E-02	9,26E+02	1,71E+00	9,28E+02	1,21E-04	0,912
	9,00E-02	9,22E+02	1,63E+00	9,24E+02	1,26E-04	0,9153
	9,50E-02	9,17E+02	1,56E+00	9,19E+02	1,31E-04	0,9183
	1,00E-01	9,10E+02	1,50E+00	9,12E+02	1,37E-04	0,9212
	1,25E-01	8,67E+02	1,24E+00	8,68E+02	1,65E-04	0,9332
	1,50E-01	8,15E+02	1,06E+00	8,16E+02	1,95E-04	0,9423
	1,75E-01	7,62E+02	9,34E-01	7,63E+02	2,26E-04	0,9495
	2,00E-01	7,13E+02	8,33E-01	7,14E+02	2,60E-04	0,9554
	2,25E-01	6,68E+02	7,53E-01	6,69E+02	2,96E-04	0,9602
	2,50E-01	6,29E+02	6,88E-01	6,29E+02	3,35E-04	0,9642
	2,75E-01	5,93E+02	6,34E-01	5,94E+02	3,76E-04	0,9676

3,00E-01	5,62E+02	5,87E-01	5,63E+02	4,19E-04	4,07E-04	0,9706
3,50E-01	5,08E+02	5,13E-01	5,08E+02	5,13E-04	5,00E-04	0,9752
4,00E-01	4,63E+02	4,56E-01	4,64E+02	6,16E-04	6,03E-04	0,9788
4,50E-01	4,28E+02	4,11E-01	4,28E+02	7,28E-04	7,15E-04	0,9815
5,00E-01	3,99E+02	3,75E-01	3,99E+02	8,49E-04	8,35E-04	0,9837
5,50E-01	3,75E+02	3,44E-01	3,76E+02	9,78E-04	9,64E-04	0,9854
6,00E-01	3,55E+02	3,19E-01	3,55E+02	1,12E-03	1,10E-03	0,9868
6,50E-01	3,37E+02	2,97E-01	3,37E+02	1,26E-03	1,25E-03	0,988
7,00E-01	3,21E+02	2,78E-01	3,21E+02	1,41E-03	1,40E-03	0,989
7,50E-01	3,06E+02	2,61E-01	3,07E+02	1,57E-03	1,56E-03	0,9898
8,00E-01	2,93E+02	2,46E-01	2,94E+02	1,74E-03	1,72E-03	0,9905
8,50E-01	2,82E+02	2,33E-01	2,82E+02	1,91E-03	1,90E-03	0,9911
9,00E-01	2,71E+02	2,22E-01	2,71E+02	2,09E-03	2,08E-03	0,9916
9,50E-01	2,61E+02	2,11E-01	2,61E+02	2,28E-03	2,26E-03	0,9921
1,00E+00	2,52E+02	2,02E-01	2,52E+02	2,48E-03	2,46E-03	0,9925
1,25E+00	2,16E+02	1,65E-01	2,16E+02	3,55E-03	3,53E-03	0,994
1,50E+00	1,90E+02	1,40E-01	1,90E+02	4,79E-03	4,77E-03	0,995
1,75E+00	1,70E+02	1,21E-01	1,70E+02	6,19E-03	6,16E-03	0,9956
2,00E+00	1,54E+02	1,07E-01	1,54E+02	7,73E-03	7,70E-03	0,996
2,25E+00	1,41E+02	9,64E-02	1,41E+02	9,43E-03	9,40E-03	0,9963
2,50E+00	1,30E+02	8,75E-02	1,31E+02	1,13E-02	1,12E-02	0,9966
2,75E+00	1,22E+02	8,02E-02	1,22E+02	1,33E-02	1,32E-02	0,9968
3,00E+00	1,14E+02	7,40E-02	1,14E+02	1,54E-02	1,53E-02	0,997
3,50E+00	1,01E+02	6,42E-02	1,01E+02	2,01E-02	2,00E-02	0,9972
4,00E+00	9,13E+01	5,67E-02	9,14E+01	2,53E-02	2,52E-02	0,9974
4,50E+00	8,34E+01	5,09E-02	8,34E+01	3,10E-02	3,09E-02	0,9975
5,00E+00	7,68E+01	4,61E-02	7,68E+01	3,73E-02	3,72E-02	0,9976
5,50E+00	7,13E+01	4,22E-02	7,13E+01	4,40E-02	4,39E-02	0,9977
6,00E+00	6,66E+01	3,89E-02	6,66E+01	5,13E-02	5,12E-02	0,9978
6,50E+00	6,25E+01	3,61E-02	6,25E+01	5,90E-02	5,89E-02	0,9978
7,00E+00	5,89E+01	3,37E-02	5,90E+01	6,73E-02	6,71E-02	0,9979
7,50E+00	5,58E+01	3,16E-02	5,58E+01	7,60E-02	7,58E-02	0,9979
8,00E+00	5,30E+01	2,98E-02	5,30E+01	8,52E-02	8,50E-02	0,998
8,50E+00	5,05E+01	2,81E-02	5,05E+01	9,48E-02	9,47E-02	0,998
9,00E+00	4,82E+01	2,67E-02	4,83E+01	1,05E-01	1,05E-01	0,998
9,50E+00	4,62E+01	2,53E-02	4,62E+01	1,16E-01	1,15E-01	0,9981
1,00E+01	4,43E+01	2,41E-02	4,43E+01	1,27E-01	1,26E-01	0,9981
1,25E+01	3,70E+01	1,96E-02	3,70E+01	1,89E-01	1,88E-01	0,9982
1,50E+01	3,19E+01	1,65E-02	3,20E+01	2,62E-01	2,61E-01	0,9983
1,75E+01	2,82E+01	1,43E-02	2,82E+01	3,45E-01	3,44E-01	0,9983
2,00E+01	2,53E+01	1,26E-02	2,53E+01	4,39E-01	4,38E-01	0,9983
2,50E+01	2,11E+01	1,02E-02	2,11E+01	6,56E-01	6,55E-01	0,9984
2,75E+01	1,95E+01	9,30E-03	1,95E+01	7,79E-01	7,78E-01	0,9984
3,00E+01	1,82E+01	8,57E-03	1,82E+01	9,12E-01	9,11E-01	0,9985
3,50E+01	1,61E+01	7,40E-03	1,61E+01	1,21E+00	1,20E+00	0,9985
4,00E+01	1,44E+01	6,52E-03	1,44E+01	1,53E+00	1,53E+00	0,9985
4,50E+01	1,31E+01	5,83E-03	1,31E+01	1,90E+00	1,89E+00	0,9985
5,00E+01	1,21E+01	5,28E-03	1,21E+01	2,29E+00	2,29E+00	0,9986
5,50E+01	1,12E+01	4,82E-03	1,12E+01	2,72E+00	2,72E+00	0,9986
6,00E+01	1,05E+01	4,44E-03	1,05E+01	3,19E+00	3,18E+00	0,9986
6,50E+01	9,82E+00	4,11E-03	9,83E+00	3,68E+00	3,68E+00	0,9986
7,00E+01	9,27E+00	3,83E-03	9,28E+00	4,20E+00	4,20E+00	0,9986

7,50E+01	8,79E+00	3,59E-03	8,80E+00	4,76E+00	4,75E+00	0,9987
8,00E+01	8,37E+00	3,38E-03	8,37E+00	5,34E+00	5,33E+00	0,9987
8,50E+01	7,99E+00	3,19E-03	7,99E+00	5,95E+00	5,94E+00	0,9987
9,00E+01	7,65E+00	3,02E-03	7,66E+00	6,59E+00	6,58E+00	0,9987
9,50E+01	7,35E+00	2,87E-03	7,35E+00	7,26E+00	7,25E+00	0,9987
1,00E+02	7,07E+00	2,73E-03	7,08E+00	7,95E+00	7,94E+00	0,9987
1,25E+02	6,01E+00	2,21E-03	6,01E+00	1,18E+01	1,18E+01	0,9988
1,50E+02	5,28E+00	1,86E-03	5,29E+00	1,63E+01	1,62E+01	0,9988
1,75E+02	4,76E+00	1,60E-03	4,76E+00	2,13E+01	2,12E+01	0,9988
2,00E+02	4,36E+00	1,41E-03	4,36E+00	2,68E+01	2,67E+01	0,9988
2,25E+02	4,05E+00	1,26E-03	4,05E+00	3,27E+01	3,27E+01	0,9989
2,50E+02	3,80E+00	1,14E-03	3,80E+00	3,91E+01	3,90E+01	0,9989
2,75E+02	3,59E+00	1,04E-03	3,59E+00	4,59E+01	4,58E+01	0,9989
3,00E+02	3,42E+00	9,60E-04	3,42E+00	5,30E+01	5,30E+01	0,9989
3,50E+02	3,15E+00	8,29E-04	3,15E+00	6,83E+01	6,82E+01	0,999
4,00E+02	2,94E+00	7,30E-04	2,94E+00	8,47E+01	8,47E+01	0,999
4,50E+02	2,79E+00	6,53E-04	2,79E+00	1,02E+02	1,02E+02	0,999
5,00E+02	2,66E+00	5,90E-04	2,66E+00	1,21E+02	1,21E+02	0,9991
5,50E+02	2,56E+00	5,39E-04	2,56E+00	1,40E+02	1,40E+02	0,9991
6,00E+02	2,48E+00	4,97E-04	2,48E+00	1,60E+02	1,59E+02	0,9991
6,50E+02	2,41E+00	4,60E-04	2,41E+00	1,80E+02	1,80E+02	0,9991
7,00E+02	2,35E+00	4,29E-04	2,36E+00	2,01E+02	2,01E+02	0,9991
7,50E+02	2,31E+00	4,02E-04	2,31E+00	2,23E+02	2,22E+02	0,9992
8,00E+02	2,26E+00	3,78E-04	2,26E+00	2,44E+02	2,44E+02	0,9992
8,50E+02	2,23E+00	3,57E-04	2,23E+00	2,67E+02	2,66E+02	0,9992
9,00E+02	2,20E+00	3,38E-04	2,20E+00	2,89E+02	2,89E+02	0,9992
9,50E+02	2,17E+00	3,21E-04	2,17E+00	3,12E+02	3,12E+02	0,9992
1,00E+03	2,14E+00	3,06E-04	2,14E+00	3,35E+02	3,35E+02	0,9992
1,50E+03	2,00E+00	2,09E-04	2,00E+00	5,78E+02	5,78E+02	0,9994
2,00E+03	1,96E+00	1,59E-04	1,96E+00	8,31E+02	8,31E+02	0,9994
2,50E+03	1,94E+00	1,29E-04	1,94E+00	1,09E+03	1,09E+03	0,9995
3,00E+03	1,94E+00	1,09E-04	1,94E+00	1,35E+03	1,35E+03	0,9995
4,00E+03	1,95E+00	8,29E-05	1,95E+00	1,86E+03	1,86E+03	0,9996
5,00E+03	1,97E+00	6,73E-05	1,97E+00	2,37E+03	2,37E+03	0,9996
6,00E+03	1,99E+00	5,67E-05	1,99E+00	2,88E+03	2,87E+03	0,9997
7,00E+03	2,01E+00	4,91E-05	2,01E+00	3,37E+03	3,37E+03	0,9997
8,00E+03	2,03E+00	4,33E-05	2,03E+00	3,87E+03	3,87E+03	0,9997
9,00E+03	2,05E+00	3,88E-05	2,05E+00	4,36E+03	4,36E+03	0,9997
1,00E+04	2,07E+00	3,51E-05	2,07E+00	4,84E+03	4,84E+03	0,9998

Electron	Chemical Composition of Human Body			
	Stopping Power			Density Effect Parameter
	Kinetic Energy (MeV)	Collision	Radiative	Total
1,00E-02	2,22E+01	3,84E-03	2,22E+01	0,00E+00
1,50E-02	1,62E+01	3,89E-03	1,62E+01	0,00E+00
2,00E-02	1,30E+01	3,92E-03	1,30E+01	0,00E+00
2,50E-02	1,09E+01	3,93E-03	1,09E+01	0,00E+00
3,00E-02	9,50E+00	3,95E-03	9,50E+00	0,00E+00
3,50E-02	8,46E+00	3,96E-03	8,46E+00	0,00E+00
4,00E-02	7,65E+00	3,97E-03	7,66E+00	0,00E+00

4,50E-02	7,02E+00	3,99E-03	7,02E+00	0,00E+00
5,00E-02	6,50E+00	4,00E-03	6,50E+00	0,00E+00
6,00E-02	5,71E+00	4,03E-03	5,71E+00	0,00E+00
7,00E-02	5,13E+00	4,07E-03	5,13E+00	0,00E+00
8,00E-02	4,68E+00	4,11E-03	4,69E+00	0,00E+00
9,00E-02	4,33E+00	4,15E-03	4,34E+00	0,00E+00
1,00E-01	4,05E+00	4,20E-03	4,06E+00	0,00E+00
1,50E-01	3,19E+00	4,46E-03	3,19E+00	0,00E+00
2,00E-01	2,75E+00	4,77E-03	2,75E+00	0,00E+00
2,50E-01	2,49E+00	5,11E-03	2,49E+00	0,00E+00
3,00E-01	2,32E+00	5,47E-03	2,32E+00	0,00E+00
3,50E-01	2,20E+00	5,87E-03	2,21E+00	0,00E+00
4,00E-01	2,12E+00	6,29E-03	2,12E+00	0,00E+00
4,50E-01	2,05E+00	6,74E-03	2,06E+00	0,00E+00
5,00E-01	2,00E+00	7,20E-03	2,01E+00	2,48E-03
6,00E-01	1,93E+00	8,19E-03	1,94E+00	4,36E-02
7,00E-01	1,89E+00	9,24E-03	1,90E+00	9,42E-02
8,00E-01	1,85E+00	1,03E-02	1,87E+00	1,50E-01
9,00E-01	1,83E+00	1,15E-02	1,84E+00	2,10E-01
1,00E+00	1,82E+00	1,27E-02	1,83E+00	2,71E-01
1,50E+00	1,79E+00	1,93E-02	1,81E+00	5,73E-01
2,00E+00	1,79E+00	2,65E-02	1,82E+00	8,47E-01
2,50E+00	1,80E+00	3,44E-02	1,84E+00	1,09E+00
3,00E+00	1,82E+00	4,26E-02	1,86E+00	1,30E+00
3,50E+00	1,83E+00	5,12E-02	1,88E+00	1,50E+00
4,00E+00	1,84E+00	6,00E-02	1,90E+00	1,67E+00
4,50E+00	1,85E+00	6,91E-02	1,92E+00	1,82E+00
5,00E+00	1,86E+00	7,84E-02	1,94E+00	1,97E+00
6,00E+00	1,88E+00	9,76E-02	1,98E+00	2,22E+00
7,00E+00	1,90E+00	1,17E-01	2,02E+00	2,44E+00
8,00E+00	1,92E+00	1,38E-01	2,05E+00	2,64E+00
9,00E+00	1,93E+00	1,59E-01	2,09E+00	2,81E+00
1,00E+01	1,94E+00	1,80E-01	2,12E+00	2,97E+00
1,50E+01	1,99E+00	2,90E-01	2,28E+00	3,61E+00
2,00E+01	2,02E+00	4,04E-01	2,42E+00	4,08E+00
2,50E+01	2,04E+00	5,22E-01	2,56E+00	4,46E+00
3,00E+01	2,06E+00	6,42E-01	2,70E+00	4,79E+00
3,50E+01	2,07E+00	7,64E-01	2,84E+00	5,06E+00
4,00E+01	2,09E+00	8,86E-01	2,97E+00	5,31E+00
4,50E+01	2,10E+00	1,01E+00	3,11E+00	5,53E+00
5,00E+01	2,11E+00	1,13E+00	3,24E+00	5,73E+00
6,00E+01	2,13E+00	1,39E+00	3,51E+00	6,07E+00
7,00E+01	2,14E+00	1,64E+00	3,78E+00	6,37E+00
8,00E+01	2,15E+00	1,89E+00	4,05E+00	6,63E+00
9,00E+01	2,16E+00	2,15E+00	4,31E+00	6,86E+00
1,00E+02	2,17E+00	2,41E+00	4,58E+00	7,06E+00
1,50E+02	2,21E+00	3,71E+00	5,92E+00	7,86E+00
2,00E+02	2,23E+00	5,03E+00	7,26E+00	8,43E+00
2,50E+02	2,25E+00	6,35E+00	8,60E+00	8,88E+00
3,00E+02	2,26E+00	7,68E+00	9,95E+00	9,24E+00
3,50E+02	2,28E+00	9,02E+00	1,13E+01	9,55E+00
4,00E+02	2,29E+00	1,04E+01	1,26E+01	9,81E+00

4,50E+02	2,30E+00	1,17E+01	1,40E+01	1,01E+01
5,00E+02	2,31E+00	1,30E+01	1,53E+01	1,03E+01
6,00E+02	2,32E+00	1,57E+01	1,81E+01	1,06E+01
7,00E+02	2,34E+00	1,84E+01	2,08E+01	1,09E+01
8,00E+02	2,35E+00	2,11E+01	2,35E+01	1,12E+01
9,00E+02	2,36E+00	2,38E+01	2,62E+01	1,14E+01
1,00E+03	2,37E+00	2,65E+01	2,89E+01	1,16E+01

A2. Calculation of density atmospheric profile

Altitude (m)	Density (10⁻¹kg/m³)
0	12,25
1000	11,12
2000	10,07
3000	9,093
4000	8,194
5000	7,364
6000	6,601
7000	5,9
8000	5,258
9000	4,671
10000	4,135
15000	1,948
20000	0,8891
25000	0,4008
30000	0,1841
40000	0,03996
50000	0,01027
60000	0,003097
70000	0,000828
80000	0,000185

Bibliography

- NIST, "estar" application, <http://physics.nist.gov/PhysRefData/Star/Text/ESTAR.html>
- Flight Plan Database, <https://flightplandatabase.com/plan/347165>
- "Beta Decay". *Lbl.gov*. (2000)
- Anatomy & Physiology, Connexions Web Site, <http://cnx.org/content/col11496/1.6/>, (2013)
- NASA's Open Data Portal, <https://data.nasa.gov/>
- NOAA Space weather prediction center- GOES electron flux data
<http://www.swpc.noaa.gov/products/aurora-30-minute-forecast>
<http://services.swpc.noaa.gov/text/aurora-nowcast-map.txt>
- NOAA POES Hemispheric Power
https://kahala2.ccmc.gsfc.nasa.gov/support/ILWS/MATERIALS/iswa_wiki/index.php/NOAA_POES_Hemispheric_Power.html
- HPS, <https://hps.org/publicinformation/ate/faqs/commercialflights.html>
- Centers for disease Control and Prevention,
https://www.cdc.gov/nceh/radiation/air_travel.html
- P. T. Newell, T. Sotirelis, J. M. Ruohoniemi, J. F. Carbary, K. Liou, J. P. Skura, C. I. Meng, C. Deehr, D. Wilkinson, and F. J. Rich, "OVATION: Oval variation, assessment, tracking, intensity, and online nowcasting", 2002
- Model Catalog and Archive <https://ccmc.gsfc.nasa.gov/modelweb/>
http://www.engineeringtoolbox.com/standard-atmosphere-d_604.html
- Federal Aviation Administration, Aviation Data & Statistics,
https://www.faa.gov/data_research/aviation_data_statistics/
- Sophie Le Caër (2011), "*Water Radiolysis: Influence of Oxide Surfaces on H₂ Production under Ionizing Radiation*", *Water* 2011, 3, 235-253
- Symeopoulos B. (2016), "*Radiobiology for undergraduate students*", University of Patras
- BBC News, "Natural bleach "key to healing" " (2009)
- Niethammer, Philipp; Clemens Grabher, A. Thomas Look & Timothy J. Mitchison (2009), "*A tissue-scale gradient of hydrogen peroxide mediates rapid wound detection in zebrafish*", *Nature* 459 (7249): 996–999
- Veal EA, Day AM, Morgan BA (2007), "*Hydrogen peroxide sensing and signaling*", *Mol. Cell* 26: 1–14.
- Weindruch, Richard (1996), "*Calorie Restriction and Aging*", *Scientific American*: 49–52.
- Giorgio M, Trinei M, Migliaccio E, Pelicci PG (2007), "*Hydrogen peroxide: a metabolic by-product or a common mediator of ageing signals?*", *Nat. Rev. Mol. Cell Biol.* 8: 722–728.

López-Lázaro M (2007), *“Dual role of hydrogen peroxide in cancer: possible relevance to cancer chemoprevention and therapy”*, Cancer Lett. 25 : 1–8

Rapoport, R.; Hanukoglu, I.; Sklan, D. (1994), *“A fluorimetric assay for hydrogen peroxide, suitable for NAD(P)H-dependent superoxide generating redox systems.”*, Anal Biochem 218: 309–13.

Schrempp L., Sizmann A., Luftfahrt B. (2012), *“Shielding Cosmic Radiation In Air Traffic”*

Beatty J.J, Matthews J. (2011) (revised August 2009 by T.K. Gaisser and T. Stanev), *“Cosmic Rays”*

R. A. Leske, R. A. Mewaldt, and E. C. Stone California Institute of Technology, Pasadena, California T. T. von Rosenvinge NASA Goddard Space Flight Center, Greenbelt, Maryland , *“Observations of geomagnetic cutoff variations during solar energetic particle events and implications for the radiation environment at the Space Station”* , JOURNAL OF GEOPHYSICAL RESEARCH, VOL. 106, NO. A12, PAGES 30,011-30,022, DECEMBER 1, 2001

B. T. Kress, C. J. Mertens, and M. Wiltberger, *“Solar energetic particle cutoff variations during the 29–31 October 2003 geomagnetic storm”*, SPACE WEATHER, VOL. 8, S05001, 2010

<http://navyaviation.tpub.com/14018/css/Metallic-Materials-34.htm>

Sophie Le Caër (2011) *“Water Radiolysis: Influence of Oxide Surfaces on H₂ Production under Ionizing Radiation”* Water 2011, 3, 235-253;

Giorgio M, Trinei M, Migliaccio E, Pelicci PG (2007), *“Hydrogen peroxide: a metabolic by-product or a common mediator of ageing signals?”*, Nat. Rev. Mol. Cell Biol. 8: 722–728.

López-Lázaro M (2007), *“Dual role of hydrogen peroxide in cancer: possible relevance to cancer chemoprevention and therapy”*, Cancer Lett. 25 : 1–8

Rapoport, R.; Hanukoglu, I.; Sklan, D. (1994), *“A fluorimetric assay for hydrogen peroxide, suitable for NAD(P)H-dependent superoxide generating redox systems.”*, Anal Biochem 218: 309–13.)

Symeopoulos B. (2016), *“Radiobiology for undergraduate students”*, University of Patras

Hajo Zeeb *et al* 2012 *J. Radiol. Prot.* **32** N15)

J. M. Thomas, R. S. Bogard (1994) *“Technical Basis for Beta Skin Dose Calculations at the Y-12 Plant”* Oak Ridge, Tennessee 37831-8169

<http://www.ornl.gov/ptp/PTP%20Library/library/Subject/Dosimetry/dosimetryr1.pdf>